

Strain Sensitivity of Li-ion Conductivity in β -Li₃PS₄ Solid Electrolyte

Pjotr Žgans¹ and Bilge Yildiz^{1,2,*}

¹Department of Materials Science and Engineering, Massachusetts Institute of Technology, 77 Massachusetts Avenue, Cambridge, Massachusetts 02139, USA

²Department of Nuclear Science and Engineering, Massachusetts Institute of Technology, 77 Massachusetts Avenue, Cambridge, Massachusetts 02139, USA

 (Received 22 December 2021; revised 27 May 2022; accepted 1 June 2022; published 21 July 2022)

Strain is present at the interfaces of solid electrolytes with the cathode and the anode in solid-state batteries due to interfacial reactions and due to volumetric expansion and contraction of the electrodes during battery charging and discharging cycles. This work quantifies the effect of elastic strain on Li-ion diffusion in a model solid electrolyte, β -Li₃PS₄, by using *ab initio* molecular dynamics (AIMD). We find that the strain tensors which compress the *c* axis (+2% *a-b*, -2% *a-c*, -2% *b-c*, -2% isotropic) increase the Li-ion diffusivity, and the strain tensors which stretch the *c* axis (-2% *a-b*, +2% *a-c*, +2% *b-c*, +2% isotropic) reduce it. Ionic conductivity increases by 2–14-fold with a reduction in activation energy for *c*-axis compressive strains and decreases by 1–14-fold with an increase in activation energy for *c*-axis tensile strains at room temperature. The *c*-axis compression increases disorder in the lattice and promotes jumps along all migration pathways. In particular, the Li 4*c* site occupancy increases from about 3% to 6% (at 500 K), thus creating more vacancies at otherwise fully occupied and bottleneck 8*d* and 4*b* sites. The *c*-axis compression also reduces the distance between the 8*d* and 4*b* sites, thus increasing Coulomb repulsion between these sites. Increased Coulomb repulsion can destabilize Li at the 8*d* and 4*b* sites, promoting reduced occupancy and increased diffusivity associated with these sites. The results show that elastic strain can promote Li disorder and superionic conductivity, with an effect on Li-ion diffusion comparable to that of chemical substitution, and is important to consider for an accurate understanding and prediction of the solid-state Li-ion battery interface properties.

DOI: [10.1103/PRXEnergy.1.023003](https://doi.org/10.1103/PRXEnergy.1.023003)

I. INTRODUCTION

Fast ionic conductivity is important for efficient operation of solid-state ionic devices, including all-solid-state lithium-ion batteries [1], solid-oxide fuel cells [2], proton-conducting membranes [3], and electrochemical analog programmable resistors [4]. While solid-state batteries offer better safety and higher energy density, the Li-ion conductivity of solid electrolytes remains lower than that of liquid organic electrolytes, limiting their charging rate and power density. The ionic conductivity of known lithium-ion-conducting solid-state electrolytes lies within 10⁻⁹–10⁻² S/cm at room temperature [5], with conductivities above 10⁻³ S/cm being desirable to enable practical applications. Solid electrolytes must also satisfy

chemical, electrochemical, mechanical, and thermal stability [6], which narrows down the set of viable electrolytes. The ionic conductivity of known electrolytes is tuned by chemical substitution and new materials are being explored for their ability to conduct Li ions [7–9].

Strain engineering presents new ways of tuning ionic conductivity in solids. Elastic strain is known to alter the mobility of holes and electrons in semiconductors [10] and to reduce band gaps [11,12]. Elastic strain can also facilitate ion transport in oxides through an increase in migration volume and decrease in metal-oxygen bond strengths [13–15]. In principle, the desired strain can be achieved through epitaxial growth of thin films on a substrate with a particular lattice mismatch [16,17], through generating electrostrictive strain in a substrate material [18], or by nanomechanical manipulation [12,19]. Accurate modulation of strain is far from trivial for practical applications of ion conductors.

Importantly, the battery charging (discharging) process often leads to volumetric expansion (contraction) of the cathode and anode materials, thus introducing mechanical strain at the interface [20–24]. Interface strains also arise as a result of interfacial reactions between the solid

*byildiz@mit.edu

Published by the American Physical Society under the terms of the [Creative Commons Attribution 4.0 International](https://creativecommons.org/licenses/by/4.0/) license. Further distribution of this work must maintain attribution to the author(s) and the published article's title, journal citation, and DOI.

electrolyte and the cathode or anode [22,25–28]. Interface-induced stresses extending into the solid electrolyte have been detected and quantified in several systems. Although stress decreases with distance from the interface, stress experienced by the electrolyte can be substantial [22,25,29]. Continuum modeling of the stress distribution in the LiCoO₂/LiPON/Si solid-state battery shows that (i) stress can reach about 1 GPa at the electrode-electrolyte interfaces during the charging process [25], with about 0.1–1 GPa stress extending into the LiPON electrolyte within at least a few nm [25]; and (ii) electrolyte decomposition can cause severe stress profiles in the order of about 10 GPa at the interface, with about 1 GPa stress extending into the electrolyte within about 100 nm [25]. Similarly, about 1 GPa stress extending into about 1 μm was reported for the Li_{1.3}Ti_{1.7}Al_{0.3}(PO₄)₃ solid electrolyte during the charging process in a composite cathode [29]. Likewise, continuum modeling of the Li_{1+x}Al_xGe_{2-x}(PO₄)₃/Li interphase growth shows about 0.1 GPa stress extending within about 100 μm into the electrolyte region [22]. In addition, compressive strains as large as 5%–10% were observed in Li_{0.33}La_{0.56}TiO₃ electrolyte at the vicinity of the epitaxial interface with a Li-rich layered electrode [30]. The anode and cathode layers also sustain large stress levels during charging and discharging processes. For example, compressive stress as high as 1.5 GPa was reported in Si thin films during galvanostatic cycling (0.01–1.5 V vs Li/Li⁺ at 50 μA cm⁻²) [31]. Similarly, about 0.4 GPa compressive stress was reported for V₂O₅ thin films (4.0–2.8 V vs Li/Li⁺ at 6 μA cm⁻²) [32]. With such high levels of stress, and respective strains in the order of about 1% (assuming ~30 GPa bulk modulus of a sulfide electrolyte [33] at a hydrostatic stress of 1 GPa for simplicity), it is reasonable to expect changes in the ionic conductivity of the electrolyte and electrode materials near their interface, as well as of the solid-electrolyte interphases (SEIs) [34,35]. To determine whether the effect of strain is beneficial or detrimental, it is important to quantify its impact on Li-ion conductivity and the underlying mechanism.

A simplified understanding of the way strain affects ionic conductivity, as deduced from the literature, is that a small tensile strain usually facilitates ion transport, while compressive strain impedes it. Tensile strain was found to accelerate ion conduction in archetypal lithium- and oxygen-ion conductors, such as Li₁₀GeP₂S₁₂ (LGPS) [36,37], Y-ZrO₂ [13], CeO₂ [14,38], and perovskite oxides [39]. In oxides, such a beneficial effect of tensile strain is rationalized in terms of increased volume along the migration path and decreased metal-oxygen bonding strength, which together facilitate migration [13].

However, in some materials, ionic conductivity increases upon compression not tension. Specifically, one should consider the activation enthalpy of ion diffusion: $\Delta H_a = \Delta E_a + p\Delta V_a$, where ΔE_a is the activation energy (without

strain) and ΔV_a is the activation volume [14]. Materials with a negative activation volume increase diffusivity under compression (and decrease diffusivity under tension). Negative activation volumes are found in Li-β-Al₂O₃ [40], Al-doped Li₇La₃Zr₂O₁₂ (Al-LLZO) [41], and many Ag-ion electrolytes (β-AgI, γ-AgI, Ag₃SI, Ag₃SBr) [42]. Compressive strain may lead to cation-disordered super-ion-conducting phases in Cu₂Se and Li₂Se through slight stabilization of high-energy sites [43]. Although positive activation volumes are reported more frequently [42], the activation volume of many materials is still unknown [42]. In general, activation volume depends on the material, composition, and even the migrating ion. Thus, the ionic conductivity of Li-, Na-, and K-β-Al₂O₃, respectively, decreases, remains unchanged, and increases under hydrostatic compression ($\Delta V_a = -0.7, \sim 0, +1.3$ cm³/mol, respectively) [40].

In the most general form, one should consider activation enthalpy as a function of stress: $\Delta H_a - \Delta E_a = -tr(\boldsymbol{\sigma} \cdot \boldsymbol{\Delta V}_a) = -(\sigma_{xx}\Delta V_{xx} + \sigma_{yy}\Delta V_{yy} + \sigma_{zz}\Delta V_{zz})$, where σ_{ii} and ΔV_{ii} are the elements of, respectively, stress and activation volume tensors [44]. Therefore, not only isotropic (or hydrostatic) strain should be considered, but also biaxial and uniaxial strains, both compressive and tensile, and shear strains, as they all influence ionic conductivity, which is not trivial to foresee quantitatively.

Atomistic simulations are useful in the characterization of the intrinsic strain effect, by “isolating” the role of strain from other factors affecting conductivity in an experimental setup [45]. For example, biaxial and uniaxial strain were shown to substantially change Li-migration barriers in LiCoO₂ [46,47], LiFePO₄ [48], and LiMnSiO₄ [49] cathode materials: up to ±0.1 eV changes for a given migration path were reported at 1% strain [we further use (eV/%) units]. Such a large change in a barrier corresponds to 50-fold increase ($e^{0.1 \text{ eV}/kT}$) of diffusion at room temperature. However, one has to be careful in assessing the relative change in Li-ion diffusivity quantitatively, since multiple different types of migration paths can be affected differently by strain [50], and so, direct simulations of diffusivity from molecular dynamics simulations would be more accurate [48].

The assessment of the strain effect on Li-ion conductivity may be challenging due to the complexity of Li diffusion. Superionic conductors often have a large concentration of diffusing entities (Li ions), which interact strongly in a confined lattice framework (“frustration”) [51]. They often have multiple Li sites (which may be partially occupied, i.e., disordered) and migration pathways, display correlated ion motion [52–57], and coupling of Li migration with the anion sublattice (e.g., rotation of polyatomic groups [58,59]). These features are typical for superionic conductors in general: Na [60], Ag [61], and F [62]. Therefore, collective simulations, for example, by *ab initio* molecular dynamics (AIMD), is more suitable than

TABLE I. The relative change in activation energy of Li-ion conduction per 1% strain, $\Delta E/\Delta \varepsilon$ (eV/%), and the relative change in Li-ion conductivity under strain with respect to the unstrained state, $\sigma_\varepsilon/\sigma_0$, at room temperature, both derived from AIMD simulations. “Iso.” and “uniax.” mean isotropic and uniaxial strains, respectively. For uniaxial strain, barrier and conductivity changes are listed for both along the axis (c) and in the perpendicular plane (a - b).

Electrolyte	Strain	$\Delta E/\Delta \varepsilon$ (eV/%)	$\sigma_\varepsilon/\sigma_0$	Refs.
LGPS	iso., -1%	-0.05, -0.06	0.13, 0.58	[36,41]
	iso., +2%	-0.02, -0.02	3.4, 4.8	[36,41]
	uniax. c , +4%	-0.005 (a - b plane)	3 (a - b plane)	[37]
		-0.03 (c axis)	14 (c axis)	[37]
Al-LLZO	iso., -1%	+0.09	3 (total)	[37]
	iso., +1%	+0.02	13	[41]
				0.7

calculating the migration barrier for a given migration path to assess the effect of elastic strain on ion conductivity in superionic conductors.

AIMD simulations of Li-ion conduction under strain were reported for LGPS [36,37,41] and Al-LLZO [41] (Table I). For LGPS, conductivity increases under isotropic tension, while for Al-LLZO it increases under isotropic compression. The activation enthalpy change is larger under compression, reaching -0.06 eV/% (LGPS) and $+0.09$ eV/% (Al-LLZO). This corresponds to, respectively, an 8-fold decrease and 13-fold increase of conductivity at room temperature ($\varepsilon = -1\%$). The effect of anisotropic uniaxial strain was also reported (LGPS [37]) but was less pronounced than that of the isotropic one. The opposite behavior of LGPS and LLZO under strain was attributed to the fact that Li-S bonds tend to increase at the transition state of Li migration (LGPS), while Li-O bonds shrink at the transition state (LLZO) [41].

To advance our understanding of how elastic strain affects the Li-ion conductivity of solid electrolytes, and find out if any general conclusions regarding the mechanism of the strain effect on superionic conductors can be drawn, we have investigated Li-ion diffusivity in an archetypal electrolyte, β -Li₃PS₄, by means of AIMD. We articulate the following constraints of this study:

- (1) consider the intrinsic effect of strain at stoichiometric composition. Strain can introduce off-stoichiometry, which also influences ionic transport [63], but we do not consider strain coupling to Li stoichiometry, to space charges, or to electrochemical concentration gradients in this study;
- (2) focus on small elastic strain and not on large strains that cause plastic deformation by creating extended defects;
- (3) consider biaxial strain, as this is relevant to interfacial strain;
- (4) consider as low a temperature interval as possible (500–650 K); at higher temperatures (~ 1000 K), the Li-ion diffusion mechanism might be somewhat

different, while simulations at room temperature are not feasible due to slow transport;

- (5) consider an archetypal ion conductor with a simple structure; as discussed, fast Li-ion conductors, such as LGPS and LLZO, have received sizable attention, yet assessment of the strain effect on the conductivity of simpler structures can be helpful in resolving the governing mechanisms more clearly.

The selected model material, β -Li₃PS₄, meets the above-mentioned criteria. It has a simple structure, good Li-ion conductivity at room temperature ($\sim 10^{-4}$ S/cm), and represents the sulfide-based electrolyte family with known correlated Li-ion motion [63]. Its ionic conductivity (without strain) is well studied. The crystal structure of orthorhombic β -Li₃PS₄ is shown in Fig. 1. The conventional cell contains 4 formula units (4Li₃PS₄), with 12 Li-ions distributed over a total of 16 Li sites (8*d*, 4*b*, 4*c*). The 8*d* and 4*b* sites are almost fully occupied and the 4*c* site is nearly empty [63]. Various migration pathways are active and contribute to Li transport [63]: connections between the neighboring 4*b*-4*c*, 8*d*-4*c*, and 8*d*-4*b* sites are especially facile, while the 8*d*-8*d* jumps along the a axis are less frequent [63]. Diffusion can be enhanced by Li off-stoichiometry achieved through chemical substitution [63,66,67].

Here, by means of AIMD simulations, we show that elastic biaxial strain has a significant effect on diffusivity. We find that strains which compress the c axis (+2% a - b , -2% a - c , -2% b - c) increase diffusivity, while strains which stretch the c axis (-2% a - b , +2% a - c , +2% b - c) decrease it. The increase or decrease of diffusivity is about twofold at 500 K. Diffusivity enhancement arises from an increase of disorder and nearly even acceleration of all migration pathways. Due to compression of the c axis, Li at 4*c* sites becomes more stable, increasing the occupancy from about 3% to 6%, and the corresponding concentration of Li vacancies at the 8*d* and 4*b* sites increases from about 1% to 2%. The doubling of the Li vacancies at the 8*d* and 4*b* sites increases the diffusion coefficient by about

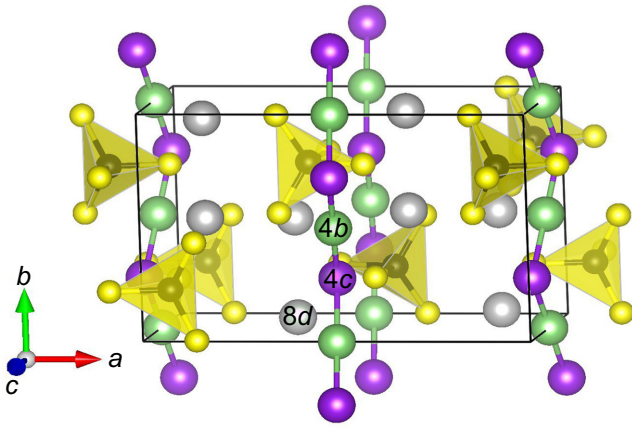


FIG. 1. β - Li_3PS_4 orthorhombic unit cell ($Pnma$ space group, $oP32$ [64]). PS_4 tetrahedra are shown in yellow (P is black at the center of the tetrahedron). Li sites: $8d$, gray; $4b$, green; $4c$, violet. Conventional cell shown in this figure contains 4 formula units ($4\text{Li}_3\text{PS}_4$), with 12 Li ions distributed over a total of 16 sites ($8d$, $4b$, $4c$). $8d$ and $4b$ sites are almost fully occupied and the $4c$ site is almost empty [63]. Li-ion diffusion is especially fast along the facile $4b$ - $4c$ chain, but other pathways also contribute to overall transport ($8d$ - $4c$, $8d$ - $4b$ and $8d$ - $8d$) [63]. In this and further figures, we use VESTA software for visualization of crystal structures [65].

twofold. For strains that stretch the c axis and reduce the Li-ion diffusivity, the concentration of Li vacancies at the $8d$ and $4b$ sites, and occupancy of Li at the $4c$ site, generally decrease. Extrapolations down to room temperature show that under ambient conditions strain can increase diffusivity by up to 1 order of magnitude for beneficial strains ($+2\%$ a - b , -2% a - c , -2% b - c) and decrease diffusivity by up to 1 order of magnitude for detrimental strains (-2% a - b , $+2\%$ a - c , $+2\%$ b - c). We observe that the magnitude of the strain effect on conductivity is comparable to the effect of chemical substitution in this material [63]. The creation of vacancies at stable sites ($8d$, $4b$) and increase of Li occupancy at the high-energy sites by strain is similar to variation of the Li stoichiometry achieved by chemical substitution [63]. The enhancement of ionic conductivity by strain through increased disorder can also be compared with other materials, where population of the high-energy sites leads to superionic conductivity (Li_2Se , Cu_2Se , AgI) [43,68].

We suggest the following explanation for strain enhancement. We observe that beneficial strains shorten the Li-Li distance between the $8d$ and $4b$ sites, thus leading to stronger Coulomb repulsion, which, in turn, slightly destabilizes Li occupancy at these sites. Destabilization of Li at the $8d$ and $4b$ sites increases disorder and decreases the migration energy, thus enhancing diffusivity. In principle, the effect of Coulomb repulsion and geometric frustration are well-known signatures of

superionicity [51,55,60,62], and here we highlight the connection between strain, separation distance between Li sites, diffusivity, and disorder.

II. COMPUTATIONAL METHODS

Density functional theory (DFT) calculations were carried out using the projector augmented wave method [69] and the Perdew-Burke-Ernzerhof (PBE) [70,71] exchange-correlation functional, as implemented in the Vienna *ab initio* simulation package (VASP) code [72–76]. Li $2s$, P $3s3p$, and S $3s3p$ electrons were treated as valence and calculations were non-spin-polarized. The plane-wave cut-off was set to 340 eV, ensuring a small Pulay stress in strained supercell calculations (≈ -0.2 kbar). To model β - Li_3PS_4 , a $1 \times 2 \times 2$ supercell was used for all calculations (128 atoms; $\sim 13 \times 16 \times 12 \text{ \AA}^3$). The experimental crystal structure ($Pnma$ space group) was used for initial lattice relaxations [77], and Li ions were placed onto the $8d$ and $4b$ sites ($4c$ site was empty). The convergence criterion for lattice relaxation was set to 0.01 eV/Å for forces. Brillouin zone integration was performed on the Γ -centered $2 \times 2 \times 2$ k -point mesh for static calculations, and Γ -point sampling for molecular dynamics runs.

Li-ion diffusion was quantified by means of AIMD simulations in the isothermal-isochoric (NVT) ensemble with the Nosé-Hoover thermostat [78,79], in the 650–500 K range. At each temperature, equilibrium lattice parameters were first determined in the isothermal-isobaric (NPT) simulations using the Parrinello-Rahman thermostat [80,81]: friction coefficients were set to 2 fs^{-1} for atoms and 10 fs^{-1} for lattice degrees of freedom; the fictitious supercell mass was set to 5 amu. In all AIMD simulations, 2 fs time steps were used. Equilibration runs were 20 ps long for NPT simulations and at least 10 ps long for NVT simulations. NPT production runs were about 200 ps long. The crystal structure was orthorhombic with all cell angles equal to 90° . The NPT converged lattice parameters were further used in NVT simulations. NVT production runs were about 200 ps at 650 K and about 1000 ps at 500 K, to acquire sufficient diffusion events (simulation of Li diffusion at 450 K or lower temperatures was found to be impractical due to poor statistics). For a complete list of performed AIMD simulations and respective Li diffusivities, see the Supplemental Material (Table S3) [82].

Biaxial strain, ε , was applied in NVT simulations as follows. At each temperature, the respective equilibrium lattice parameters, L_i , were strained, i.e., set to $(1 + \varepsilon)L_i$, while the strain-free lattice parameter was adjusted in steps until the NVT time-averaged stress was close to zero. In all production runs, residual stress was within ± 0.3 kbar. Calculation of errors was carried out using the blocking method [83].

Li-ion diffusivity was calculated as follows. Tracer diffusivity, D_{tr} , was calculated as

$$D_{\text{tr}} \equiv \lim_{t \rightarrow \infty} \frac{\langle |\Delta \mathbf{r}(t)|^2 \rangle}{6t} = \frac{1}{3} \int_0^\infty \langle \mathbf{v}(0) \mathbf{v}(t) \rangle dt,$$

where $\mathbf{r}(t)$ and $\mathbf{v}(t)$ are, respectively, the single-particle coordinate and the velocity at time t . The charge diffusion coefficient, D_{ch} (Li center of mass diffusion coefficient), was calculated as

$$D_{\text{ch}} = \frac{N_{\text{Li}}}{3} \int_0^\infty \langle \mathbf{V}_c(0) \mathbf{V}_c(t) \rangle dt,$$

where $\mathbf{V}_c = (1/N_{\text{Li}}) \sum_{i=1}^{N_{\text{Li}}} \mathbf{v}_i$ is the average velocity of all Li ions [84]. D_{tr} and D_{ch} were calculated from the integration of the velocity autocorrelation functions (Green-Kubo method), and error estimates were performed using the block average method [85]. Li-ion conductivity, σ , was calculated from the Nernst-Einstein equation, $\sigma = ((Z^2 e^2 C_{\text{Li}})/k_B T) D$, where Ze is the Li charge and $C_{\text{Li}} = N_{\text{Li}}/V$ is the number of Li ions per volume, and D is either tracer (D_{tr}) or charge (D_{ch}) diffusivity. Ionic conductivity calculated from the charge diffusivity explicitly accounts for ionic correlations and is more rigorous than that conventionally estimated from the tracer diffusivity [84]. However, charge diffusivities converge much slower with the length of trajectory as compared with tracer diffusivities [84,86]. Therefore, we discuss charge diffusivity only in a limited number of cases, and mostly we use tracer diffusivity results throughout the paper. The room-temperature conductivity was calculated from the D_{tr} extrapolated down to room temperature.

To calculate Li-site occupancies, we performed Bader charge analysis [87,88] on the AIMD calculated Li-ion density. Bader analysis is commonly used to assign ionic charges by partitioning the electron density of molecules and solids [87]. The advantage of Bader analysis is that it does not assume any particular form or symmetry of charge density and is therefore suitable for partitioning Li-ion density, which is highly anisotropic (see Fig. 2). Partitioning was done by finding zero-flux surfaces between atoms, with density taking a minimum on the surface and increasing along the normal [87,88]. Integration of the density within Bader volume of an atom (space enclosed within zero-flux surfaces surrounding atom) yielded atomic charge, and this gave the Li-site occupancy in our case. To calculate the number of Li-ion jumps between sites, we followed the approach outlined by de Klerk *et al.* [63], with improvements to account for strong anisotropy of Li thermal ellipsoids.

For further details regarding AIMD calculations, analysis, and result details, see the Supplemental Material (Secs. A–K) [82].

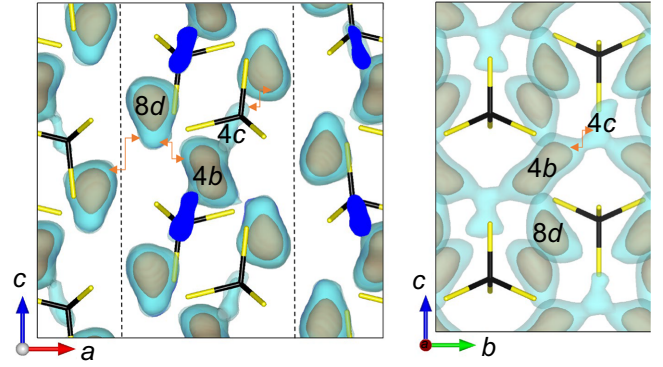


FIG. 2. Three-dimensional (3D) Li-ion density of β -Li₃PS₄ obtained from AIMD simulations at 500 K: a - c (left) and b - c (right) plane views. PS₄ groups are shown as black-and-yellow sticks. $8d$ and $4b$ sites are stable, with typical residence times of 80 and 30 ps, respectively. $4c$ is a transient site with a short 1 ps residence time. $8d$ - $4b$ - $4c$ sites form two-dimensional continuous layers (b - c layers), which are highlighted with dashed lines. Within the b - c layer, diffusion happens mainly via $4b$ - $4c$, $8d$ - $4c$, $8d$ - $4b$, and $8d$ - $8d$ nearest-neighbor jumps. Between b - c layers, diffusion happens mainly via $8d$ - $8d$ interlayer jumps.

III. RESULTS AND DISCUSSION

A. Crystal structure and site occupancies

1. β -Li₃PS₄ crystal structure

We start with a comparison of the calculated lattice parameters, unit cell volume, and thermal expansion coefficient with available experimental data. Our results are summarized in Table II. The static lattice parameters calculated by DFT are overestimated by 0.2%–1.8% and the unit cell volume by 3.6%, as compared to the experimental values at room temperature. We note that such an overestimation is typical for the PBE functional [91].

AIMD simulations in the NPT ensemble show that β -Li₃PS₄ retains an orthorhombic shape (all interaxial angles are 90°). The room-temperature lattice parameters are overestimated by 0.4%–2.9% and the unit cell volume

TABLE II. Lattice parameters, unit cell volume, and thermal expansion coefficients of orthorhombic β -Li₃PS₄. Comparison of the static DFT and AIMD (NPT) results with experimental data at room temperature.

	Expt.	DFT (static)	AIMD (300 K)
a (Å)	12.98 [89]	13.02	13.05
b (Å)	8.04 [89]	8.17	8.28
c (Å)	6.13 [89]	6.25	6.30
V (Å ³)	639.6 [89]	664.6	680.4
α_a (10 ⁻⁵ K ⁻¹)	0.5 [89]	not applicable	1.2
α_b (10 ⁻⁵ K ⁻¹)	5.2 [89]	not applicable	4.8
α_c (10 ⁻⁵ K ⁻¹)	2.5 [89]	not applicable	2.5
α_V (10 ⁻⁵ K ⁻¹)	8.1 [90]	not applicable	8.2

by 6%. The calculated thermal expansion coefficients are in good agreement with experiments, showing most pronounced expansion for the b axis, a smaller expansion along the c axis, and minor expansion along the a axis. The volumetric thermal expansion coefficient is $8.2 \times 10^{-5} \text{ K}^{-1}$ at room temperature, which is in excellent agreement with the experimentally determined value (see Table II).

We note that a negative thermal expansion along the a axis was reported from 50 to 350 °C [92]. We also note that the reported experimental lattice parameters are somewhat scattered (agree within $\sim 1\%$ [89,93,94]) and differences might be attributed to different synthesis methods, resulting structures (“nanoporous” or bulk) [95], or impurities [90].

2. Li-site occupancy and disorder

Fast ion transport is mainly possible via disorder, as is known for archetypal superionic conductors PbF_2 [96, 97], AgI [61,98,99], Bi_2O_3 [100,101], and others (see Ref. [102] for a review). Therefore, assessment of the Li sublattice disorder (site occupancy) and its change upon strain is central to this work.

In $\beta\text{-Li}_3\text{PS}_4$, three Li sites are commonly distinguished: $8d$ (tet), $4b$ (oct), and $4c$ (tet) [64]. Li-site occupancies of $\beta\text{-Li}_3\text{PS}_4$ were previously reported; however, the values were inconsistent between studies [63,64,77,89,90, 92,103]. The occupancies in experimental studies were obtained with Rietveld refinement of x-ray and neutron diffraction data [64,77,89,90,92], and the reported values for the $8d$, $4b$, and $4c$ sites were 1, 0.7, and 0.3 [64,77,90, 92] [These refs. include a single-crystal x-ray diffraction study [64], x-ray powder diffraction (XPD) [77], neutron powder diffraction (NPD) [92], and simultaneous refinement of XPD and NPD at two neutron wavelengths [90].] Occupancies of 1, 0.4, and 0.6 were also reported in one NPD study [89]. The reported Rietveld refinements show that $4b$ and $4c$ sites are partially occupied, which points to substantial disorder on these sites. By contrast, our AIMD simulations yielded practically integer occupancies (0.99, 0.99, 0.03), which means that the Li sublattice is ordered [104,105]. The discrepancy could have arisen from the fact that the reported Rietveld refinements of $\beta\text{-Li}_3\text{PS}_4$ [64,77,89,90,92] failed to address the anisotropy of Li thermal ellipsoids, which was critical for determination of the occupancies (cf. [106,107]). Li thermal ellipsoids of superionic conductors are highly anisotropic, according to nuclear density maps from AIMD [57,108] and neutron diffraction [90,106,109]. Numerous examples include LLZO [57,106,108], LGPS [57], $\beta\text{-Li}_3\text{PS}_4$ [57,90], and other compounds [57]. To restore the anisotropy of thermal ellipsoids from the Rietveld refinement a high-quality diffraction signal [106] or advanced fitting methods, such as reverse Monte Carlo, are required [107].

Anisotropy of Li thermal ellipsoids in $\beta\text{-Li}_3\text{PS}_4$ is seen from AIMD [Fig. 2 (cf. [57,90])]. The $8d$, $4b$, and $4c$ ellipsoids have complex shapes of Li-ion density, which require a delicate analysis to assign site occupancies; a crude integration “in spheres” would lead to oversimplification. In this work, we determine occupancies by Bader analysis [87,110], which is commonly used to partition the arbitrary electron density of molecules and solids and assign ionic charges [87] and is thus suitable to partition highly anisotropic Li-ion density (Fig. 2) and assign site occupancies. As seen in Fig. 2, Li-ion density at the $4c$ site is much lower than that at the $8d$ and $4b$ sites. Thus, the $4c$ site is the least stable and respective ion residency time is much shorter than those at the $8d$ and $4b$ sites.

Isotropic Li ellipsoids used in the reported Rietveld refinements [64,77,89,90,92] could lead to a high occupancy (0.3). The $4b$ thermal ellipsoids are elongated towards the $4c$ site (Fig. 2), thus part of the $4b$ site Li-ion density is wrongly assigned to the $4c$ site. Similar inaccuracy can be produced by a crude analysis of AIMD: in Ref. [103], integration of the Li density within site-centered spheres yields 0.34 occupancy of the $4c$ site (700 K), assuming the $4c$ sphere radius is 2.5 \AA [103], which clearly overlaps with two neighboring $4b$ ellipsoids. Integration within a smaller sphere radius of about 1 \AA yields about 0.08 occupancy at most (750 K) [63].

To reconcile the reported Rietveld occupancies [64,77, 90,92] and our AIMD results, we note that $\beta\text{-Li}_3\text{PS}_4$ has both configurational and “directional” Li disorder (i.e., occupancies and anisotropy of thermal ellipsoids). As discussed in the literature, occupancy and anisotropy estimated with Rietveld refinements are correlated [106,107], and our abovementioned analysis confirms this understanding. Reported Rietveld refinements impose directional isotropy [64,77,89,90,92]; therefore, the resultant occupancies display apparent disorder (0.7 of $4b$ and 0.3 of $4c$). The Bader analysis of AIMD Li density imposes no restrictions on anisotropy, and hence, the obtained occupancies reflect the order (0.995 of $4b$ and 0.025 of $4c$). We thus believe that $\beta\text{-Li}_3\text{PS}_4$ has (1) strongly anisotropic Li thermal ellipsoids, and (2) an ordered Li sublattice with virtually full $8d$ and $4b$ sites and an almost empty $4c$ site. This is valid at the temperatures of our AIMD simulations and at room temperature (for further discussion, see the Supplemental Material, Sec. D [82], and Refs. [63,93] about the order and disorder in $\beta\text{-Li}_3\text{PS}_4$).

B. Li-ion diffusion

1. Diffusion without strain

Li diffusion in $\beta\text{-Li}_3\text{PS}_4$ was investigated with AIMD simulations at 500–650 K; the calculated tracer diffusivity is shown in the Arrhenius plot of Fig. 3. We obtained an activation energy of $0.49 \pm 0.02 \text{ eV}$, and extrapolation

to lower temperatures yielded $D_{\text{tr}} = 4.9 \times 10^{-10}$ cm²/s ($\sigma = 0.06$ mS/cm) at room temperature.

Our calculated activation energy and conductivity fell within the range reported by experiments, which showed significant variability (0.22–0.49 eV, 10^{-4} – 10^{-1} mS/cm) [90,93,95,112]. However, our calculated values did not match both quantities simultaneously reported in a single experiment. The scatter in experimental literature could arise from different synthesis methods and resulting variabilities in the microstructure, such as the inclusion of glassy regions and grain boundaries [95]. Scatter also stems from different measurement techniques being used, which probe Li-ion motion on different time and length scales (see Table S1 within the Supplemental Material [82]). Previous AIMD reports showed scatter in the quantified activation energy and conductivity as well (Fig. 3). This could be attributed to short trajectories [111], different simulation temperatures [59], and excessive disorder affecting the activation energies [103].

We see that both experimental and computational studies have their own limitations, making straightforward agreement between them, so far, elusive. (For further discussion, see the Supplemental Material, Sec. F [82].) Instead, we focused on getting as accurate as possible results within our simulation model and assessed the effect of strain consistently with respect to the unstrained state in our simulations. For a proper analysis of strain effect on conductivity, we carefully converged the AIMD diffusivities and estimated errors of the Arrhenius fit (see the Supplemental Material, Sec. G [82]). In what follows, we set the reference state to be strain-free β -Li₃PS₄ with an activation energy of 0.49 eV and Li-ion conductivity of 0.06 mS/cm.

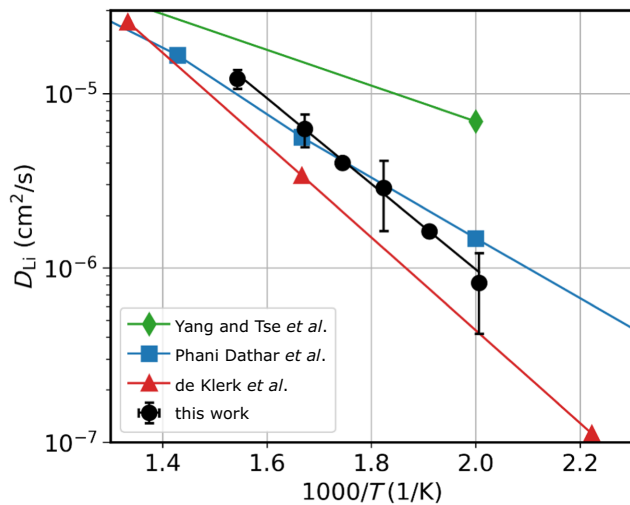


FIG. 3. Li-ion (tracer) diffusivity in β -Li₃PS₄ (without strain, $\varepsilon = 0\%$) calculated with AIMD. AIMD simulations of diffusivity from the literature are shown for comparison: Yang and Tse *et al.* [111], Phani Dathar *et al.* [103], de Klerk *et al.* [63].

2. Diffusion under strain

Here, we present and discuss the effect of strain on Li-ion diffusion in β -Li₃PS₄. We investigated the +2% and -2% biaxial strains in the *a-b*, *a-c*, and *b-c* crystallographic plains, as well as $\pm 2\%$ isotropic strain, and compared these to the unstrained case.

An Arrhenius plot of the Li-ion diffusivities calculated at 650–500 K is shown in Fig. 4(a). We see that the +2% *a-b*, -2% *a-c*, and -2% *b-c* biaxial strains, and -2% isotropic strain, increase Li-ion diffusivity compared with the unstrained case. Interestingly, all these strains decreased the *c* lattice parameter by about 2% [Fig. 4(b)]. Conversely, the -2% *a-b*, +2% *a-c*, and +2% *b-c* biaxial strains, and +2% isotropic strain, decreased the diffusivity and increased the *c* lattice parameter [Fig. 4(b)]. Thus, the strains that compressed the lattice along the *c* axis increased the Li-ion diffusivity, and those that expanded along the *c* axis decreased the Li-ion diffusivity in β -Li₃PS₄.

The effect of strain on diffusivity was more pronounced at 500 K compared with that at higher temperatures (see also Fig. S17 within the Supplemental Material [82]). Diffusivity increased by a factor of 1.7–2.6 for strains that compressed the *c* axis (+2% *a-b*, -2% *a-c*, -2% *b-c*, -2% isotropic), and decreased by a factor of 0.5–0.9 for strains that stretched the *c* axis (-2% *a-b*, +2% *a-c*, +2% *b-c*, +2% isotropic). Extrapolation down to room temperature showed an even more pronounced effect, especially for the *a-b* and *a-c* strains [Fig. 4(c); note that the error bars are large; see also the Supplemental Material, Sec. G [82]; cf. Ref. [113]]. Li-ion conductivity could change by up to 1 order of magnitude with respect to the unstrained case: for +2% *a-b*, -2% *a-c*, -2% *b-c*, and -2% isotropic strain, diffusivity increased by up to 10^1 times; for the -2% *a-b*, +2% *a-c*, +2% *b-c*, and +2% isotropic strain, diffusivity decreased by up to 10^{-1} times.

The activation energy varied linearly with strain from -2% to +2% [Fig. 5(a)], and the gradients were about |0.06|, |0.03|, and |0.00| eV/% for, respectively, *a-b*, *a-c*, and *b-c* strains (|0.01| eV/% for isotropic strain). The variation of the pre-exponential factor was likewise linear [Fig. 5(b)].

Remarkably, the isotropic strain effect was less pronounced than that of the *a-b* and *a-c* biaxial strains (strain effect decreased as follows: *a-b* > *a-c* > isotropic > *b-c*). While the figures here show only the biaxial strain effects, the effect of isotropic strain on Li-ion diffusivities are shown in the Supplemental Material, Sec. G [82].

The impact of small strain, at room temperature, could be interpolated from the Arrhenius fit in Fig. 5. Thus, 0.2% *a-b*, *a-c*, *b-c*, or isotropic strain caused about 10–30% change in Li-ion conductivity and 0.5% strain caused about 10–80% change. Notably, 0.2% strain corresponded to about 60 MPa biaxial stress in β -Li₃PS₄, which was comparable to the stack pressure [114,115] applied in

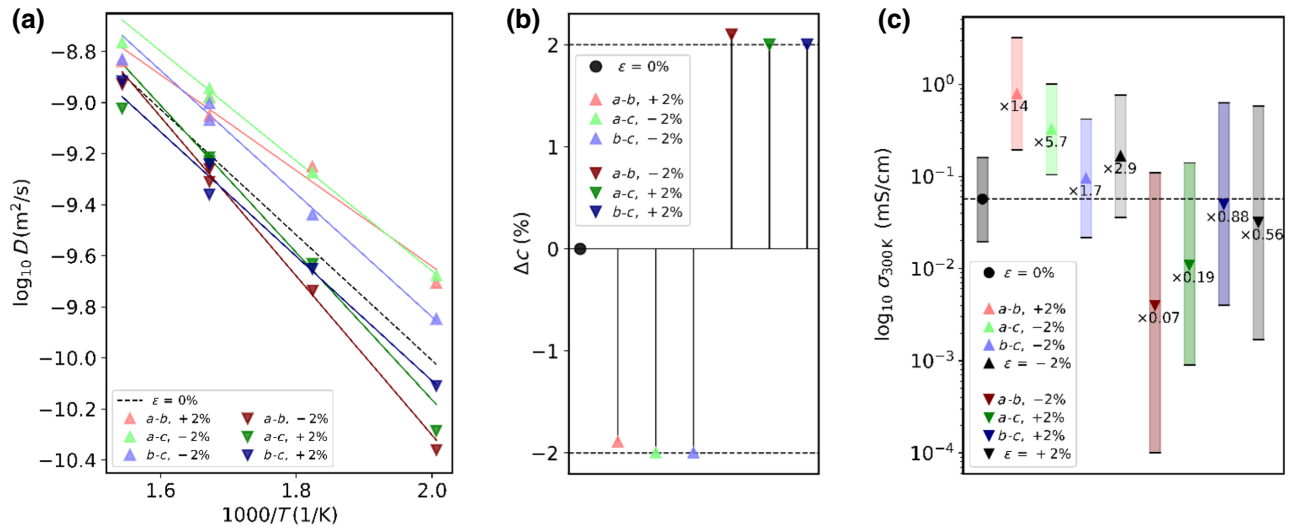


FIG. 4. Li-ion diffusivity under $\pm 2\%$ biaxial strain on the a - b , a - c , and b - c planes of $\beta\text{-Li}_3\text{PS}_4$, deduced from AIMD simulations. (a) Arrhenius plot (650–500 K). Dashed line shows strain-free diffusivity ($\epsilon = 0\%$) as a reference state. (Isotropic strain diffusivities are shown in the Supplemental Material, Sec. G [82].) (b) Relative change in c lattice parameter under biaxial strain at 500 K. (c) Li-ion conductivity extrapolated to room temperature; one standard deviation confidence intervals are highlighted; $\epsilon = -2\%$ and $\epsilon = +2\%$ label conductivities under isotropic compressive and tensile strain, respectively; text label of each marker provides the relative change in Li-ion conductivity with respect to the unstrained state ($\sigma_\epsilon/\sigma_{\epsilon=0}$ ratio).

all-solid-state Li-ion batteries. Interestingly, about 0.2% strain could appear also because of the synthesis conditions, as recently reported for ball-milled Na_3PS_4 solid electrolyte [42]. Furthermore, 0.5% strain corresponded to about 150 MPa biaxial stress in $\beta\text{-Li}_3\text{PS}_4$, and, as discussed in Sec. I, such (interfacial) stress could penetrate deep into the solid electrolyte.

Furthermore, the activation volume tensor ($\Delta \mathbf{V}_a$) could be deduced from our calculations. We fit three unknown diagonal elements, ΔV_{ii} , to the following eight equations (one for each strain): $\Delta H_a - \Delta E_a = -\text{tr}(\boldsymbol{\sigma} \cdot \Delta \mathbf{V}_a) = -(\sigma_{xx} \Delta V_{xx} + \sigma_{yy} \Delta V_{yy} + \sigma_{zz} \Delta V_{zz})$, where ΔH_a and σ_{ii} are, respectively, the activation enthalpy and stress at a given

strain, and ΔE_a is the activation energy. We thus estimated that $\Delta V_{xx} = 2 \pm 4 \text{ cm}^3/\text{mol}$, $\Delta V_{yy} = 13 \pm 5 \text{ cm}^3/\text{mol}$, and $\Delta V_{zz} = -18 \pm 5 \text{ cm}^3/\text{mol}$. The magnitudes of ΔV_{ii} reflected the response of diffusivity to strain along each crystallographic direction. Diffusivity was most sensitive to strain along the c and b axes and was least sensitive to strain along the a axis. For example, $+2\%$ a - b strain had the most pronounced effect: both the b tension and the c compression were beneficial, while the a compression had little impact ($|\Delta V_{xx}| \ll |\Delta V_{yy}| < |\Delta V_{zz}|$). The average activation volume was estimated to be $\Delta V_a = -2 \pm 3 \text{ cm}^3/\text{mol}$, which placed $\beta\text{-Li}_3\text{PS}_4$ among the few superionic conductors

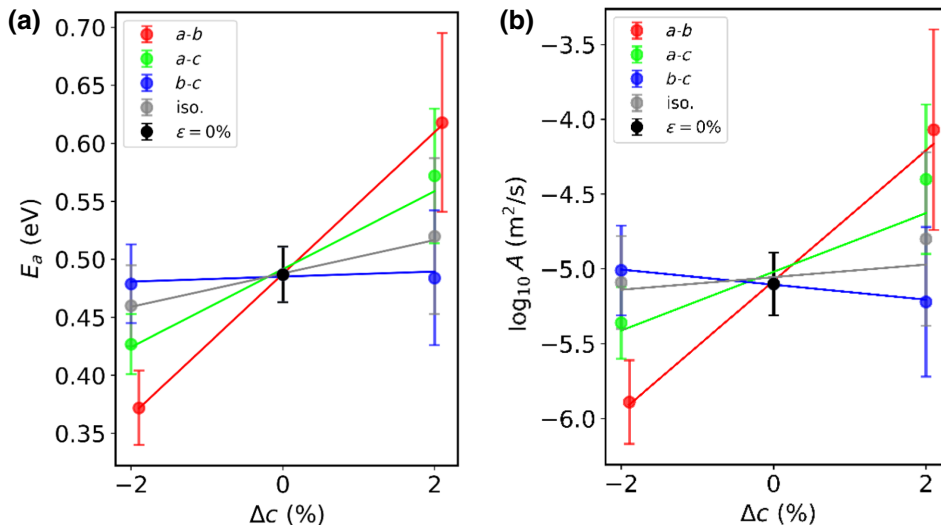


FIG. 5. (a) Activation energy, E_a , and (b) logarithm of the pre-exponential factor ($\log_{10} A$) of Li-ion diffusivity under $\pm 2\%$ isotropic and biaxial strain on the a - b , a - c , and b - c planes of $\beta\text{-Li}_3\text{PS}_4$ deduced by AIMD simulations at 500–650 K, presented as a function of the relative change in the c parameter.

with a negative activation volume known to date (e.g., β -AgI, Ag₃SI, and Li- β -Al₂O₃ having activation volumes of -5.9 , -2.3 , and -0.7 cm³/mol, respectively) [42].

C. Mechanism of strain-enhanced Li-ion diffusivity

To resolve the mechanism by which elastic strain affected Li-ion diffusivity in β -Li₃PS₄, we calculated the Li-site occupancies, analyzed Li jumps in AIMD, and calculated typical Li-ion residence times for each site. We also analyzed structural changes induced by strain.

1. Site occupancies and ion jumps

Recall that the $8d$ and $4b$ sites are almost fully occupied, and the $4c$ site is almost empty. In fact, fully occupied or completely empty sites can impede diffusion, since they impede the exchange of charge carriers (Li ions or vacancies). In a simplified picture of (vacancy-mediated) single-ion hop diffusion, what matters for facile transport is the concentration of vacancies at the $8d$ and $4b$ sites and the concentration of Li ions at the $4c$ site. The highest conductivity is expected for a fully disordered Li sublattice

(cf. Ref. [103]). Remember that beneficial strains are those that increase Li-ion diffusivity (and compress the c axis: $+2\%$ a - b , -2% a - c , -2% b - c), while detrimental strains are those that decrease diffusivity (and stretch the c axis: -2% a - b , $+2\%$ a - c , $+2\%$ b - c).

In β -Li₃PS₄, various migration pathways are active and contribute to Li transport [63] (Fig. 2). In agreement with a previous study [63], we saw that jumps were most frequent between $4b$ - $4c$, $8d$ - $4c$, and $8d$ - $4b$ neighboring sites. These jumps provided transport within the b - c layers and were often back-and-forth hops. Less frequent were $8d$ - $8d$ jumps between neighboring sites (within b - c layers) and $8d$ - $8d$ jumps between b - c layers, which contributed to long-range diffusion along the a axis. Overall, Li diffusion was facile in all three dimensions, although somewhat faster in the b - c plane and somewhat slower along the a axis. There are also other types of jumps, which are rare, and we do not consider them here for simplicity.

Remarkably, the beneficial strains that compressed the c axis promoted all these “main” jumps ($4b$ - $4c$, $8d$ - $4c$, $8d$ - $4b$, $8d$ - $8d$) (Fig. 6). An average increase in jump rate was 1.8 times at 500 K (from 1.2 times to 3.2 times), as

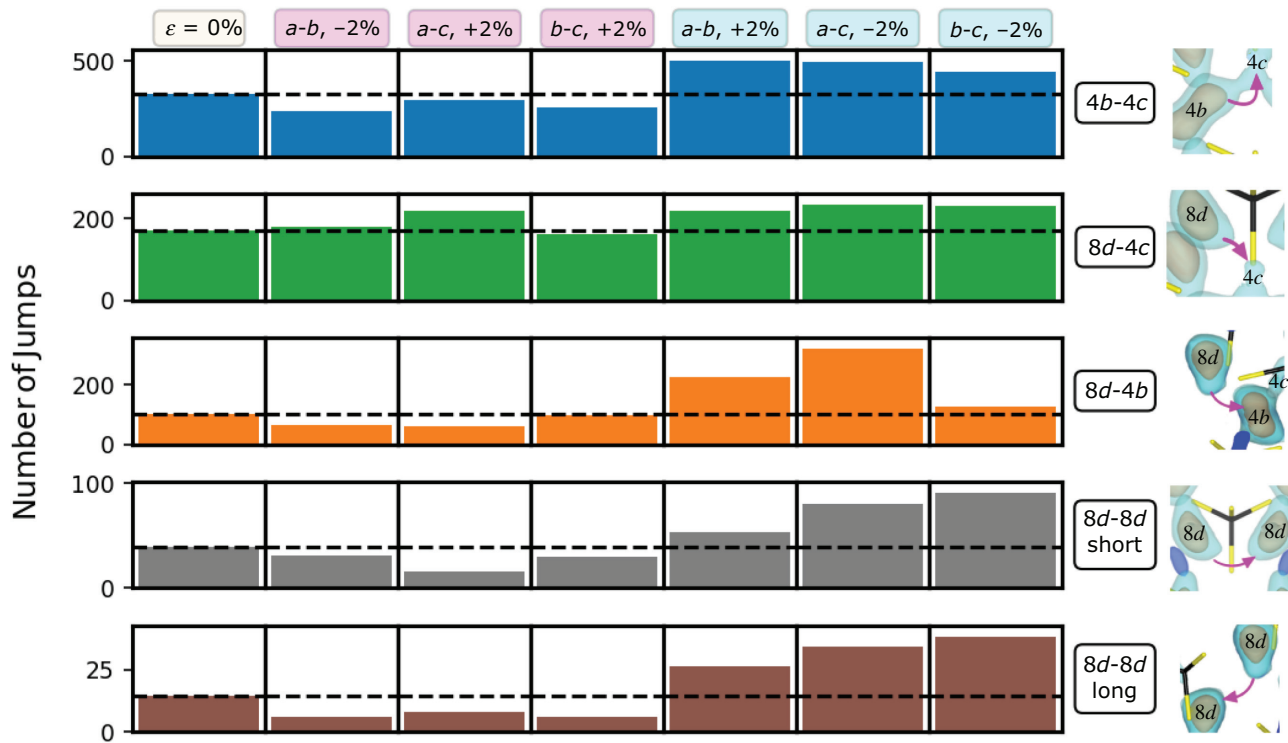


FIG. 6. Number of jumps observed during AIMD runs (500 K, 1 ns). Number of jumps in the strain-free case is shown in the first column ($\epsilon = 0\%$). Next three columns show detrimental strains (-2% a - b , $+2\%$ a - c , $+2\%$ b - c), which stretch the c axis. Last three columns show beneficial strains ($+2\%$ a - b , -2% a - c , -2% b - c), which compress the c axis. Dashed lines show number of jumps in the strain-free case as a reference. Types of jumps are as described in the main text (“ $8d$ - $8d$ short” are jumps between nearest-neighbor sites; “ $8d$ - $8d$ long” are jumps between b - c layers). For jumps between different sites ($4b$ - $4c$, $8d$ - $4c$, $8d$ - $4b$), the number of backward jumps ($4c$ - $4b$, $4c$ - $8d$, $4b$ - $8d$) is not shown (it is almost equal to the number of forward jumps, as expected in equilibrium [63]). For jumps between the same sites ($8d$ - $8d$), the total number of jumps is shown (forward and backward). We also note that only a portion of jumps contribute to a net displacement of Li ions (see the Supplemental Material, Sec. H [82]; cf. Refs. [116,117]).

calculated for beneficial strains (+2% a - b , -2% a - c , -2% b - c). For detrimental strains, an average change in jump rates was 0.8 times at 500 K (from 0.4 times to 1.3 times). This naïve averaging over different jump and strain types correlated rather well with the overall diffusivity increase presented in the previous section (2.2 times and 0.7 times for, respectively, beneficial and detrimental biaxial strains at 500 K). We also noted that the three-dimensional character of Li-ion diffusion was retained, regardless of biaxial strain type.

The acceleration of Li ion diffusion, associated with an increased number of jumps, could also be rationalized in terms of the Li-site disorder (site occupancies, Fig. 7). The beneficial strains increased the $4c$ site occupancy and increased the number of $8d$ and $4b$ site vacancies (decrease in Li occupancy). This increase in Li occupancy at $4c$ sites and in Li vacancies at $8d$ and $4b$ sites was about twofold at 500 K, which was consistent with the almost 2 times increase in the Li-ion diffusion coefficient. Detrimental strains influenced the site occupancies somewhat less markedly. For +2% a - c strain, the increase in $4c$ site occupation and increase in $8d$ and $4b$ vacancy concentrations was minor. For -2% a - b and +2% b - c strains, the $4c$ site occupation and $8d$ and $4b$ vacancy concentrations somewhat decreased (Fig. 7).

To assess the role of disorder on Li-ion conduction, i.e., increase in the $8d$ and $4b$ Li vacancy concentrations and the $4c$ Li-site occupation, we estimated the change in jump rates based only on site occupancies. In the single-hop picture of (vacancy-mediated) diffusion, the jump rate from site i to j was proportional to $p_i(1 - p_j)$, where p_i and p_j were respective site occupancies. For beneficial strains that compressed the c axis, the thus calculated average increase in Li-ion diffusion was 2.3 times at 500 K (from 1.0 to 6.6 times). For detrimental strains, the average change was 0.6 times at 500 K (from 0.0 to 1.5 times). These simple estimates of how much the Li-ion conductivity should change based on site occupancies were largely consistent with the changes in Li-ion conductivity calculated from AIMD, as presented above.

2. Site energy and stability

The changes in the Li-site occupancies could be justified by calculating the effect of strain on the site energies for Li in β -Li₃PS₄. We created a defect pair by placing one Li ion from the $8d$ site into the neighboring $4c$ site. This defect pair was associated with a site occupancy increase at $4c$ and decrease at $8d$. The placement of one $8d$ Li ion on the $4c$ site cost about 0.29 eV from static DFT

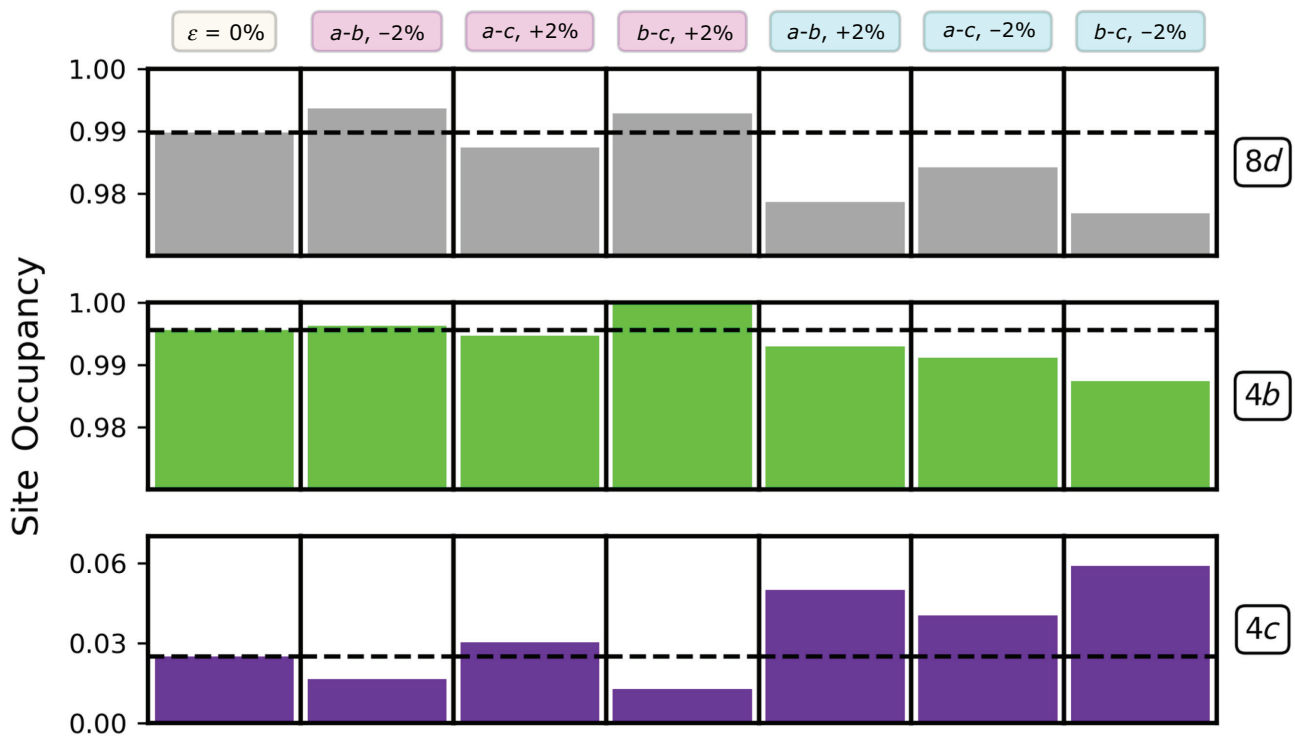


FIG. 7. Occupancy of $8d$, $4b$, and $4c$ Li-ion sites for $\pm 2\%$ biaxial strains at 500 K, calculated by Bader analysis of the Li-ion density obtained in AIMD simulations. Occupancies of sites in the strain-free case are shown in the first column ($\epsilon = 0\%$). Next three columns show detrimental strains (-2% a - b , +2% a - c , +2% b - c), which stretch the c axis. Last three columns show beneficial strains (+2% a - b , -2% a - c , -2% b - c), which compress the c axis. Dashed lines show occupation in the strain-free case.

calculations in the strain-free case. The formation energy of such $8d-4c$ defect pairs decreased by about 0.026 eV (on average) for strains that increased Li-ion conductivity (those that compressed along c) and increased by 0.014 eV (on average) for detrimental strains. The relative change in the $4c$ site occupation at 500 K could thus be estimated using a Boltzmann distribution, $\exp(-\Delta E/k_B T)$, and this gave 1.8 and 0.7 times relative changes on $4c$ site occupancy, respectively, for beneficial and detrimental strains. This was largely in agreement with the changes in the $4c$ site occupancies as a function of strain calculated from AIMD simulations presented above (Fig. 7). We also analyzed lattice relaxation after Li migration from the $8d$ to the $4c$ site. The a and b lattice parameters expanded by, respectively, +0.018 and +0.012 Å, while the c lattice parameter changed by -0.023 Å, and the total supercell volume change was positive, $+0.5$ Å³. This was consistent with our finding that compression along the c axis favored an increase in Li occupancy at the $4c$ sites (Fig. 7).

The change in site energy (stability) was also evaluated from AIMD simulations. We calculated the ion residency time (how long the Li ion stayed at a given site) and further assessed the escape barriers of Li-ion migration from a given site to another site. For strains that increased conductivity (c -axis compressive), the $8d$ and $4b$ escape barriers decreased by about 0.02 eV (on average), while the $4c$ escape barrier increased by about +0.01 eV (on average). Thus, the relative stability of the $4c$ site was increased by $-(-0.02 \text{ eV}) + 0.01 \text{ eV} = 0.03 \text{ eV}$, consistent with the static calculations. Although the stability of the $4c$ site for Li increased, it was still much less stable than $8d$ and $4b$

and remained a transient site with a short residency time of about 1 ps, as opposed to about 80 ps for $8d$ and about 30 ps for $4b$ (see the Supplemental Material, Sec. J [82], for further details).

3. Structure: Li-Li distances

We analyzed the structural changes upon strain in β -Li₃PS₄ by first looking at the radial distribution function (RDF). The analysis was complicated by the fact that each RDF peak was affected by biaxial strain, causing slight shifts of peaks, broadening or stiffening of peaks, or peak splitting. We could identify two RDF features that were common to all the strains that compressed the c axis and accelerated Li-ion conduction.

The first feature concerned the second P-P peak shown in Figs. 8(a) and 8(b); this peak was a superposition of several crystallographic distances in the 6–7 Å range, which formed a 3D framework. First, compression of the c axis reduced the P-P distances parallel to c ; therefore, the component at the left of this peak (separated as a shoulder) shifted to the left. Second, the whole second P-P peak was broadened [Fig. 8(a)]. In contrast, detrimental strains that expanded the c axis sharpened this peak [Fig. 8(b)]. Peak broadening implied that, overall, the P framework was becoming more “geometrically disordered.” Such an increased “disorder” of P-P bond population might be associated with a more flexible structure, and therefore, facilitated Li diffusion. The flexibility of the lattice is known to enhance ion diffusion in solids [118,119]. We note that these P-P distances (6–7 Å) are not necessarily

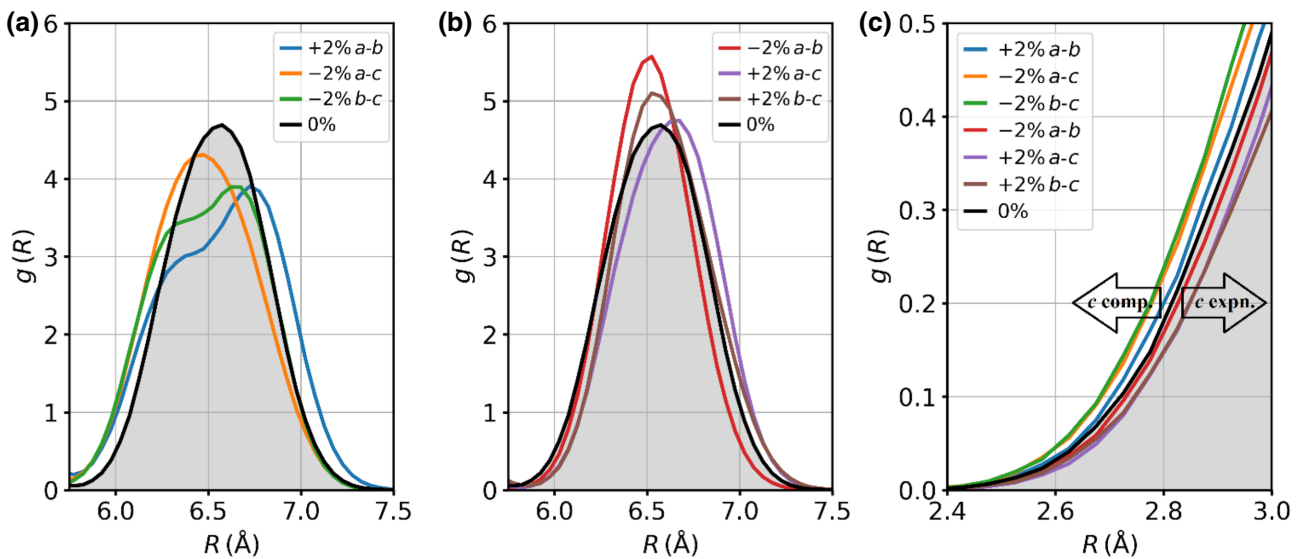


FIG. 8. Radial distribution function of P-P distances in β -Li₃PS₄ under biaxial strains, which (a) compress the c axis and (b) expand the c axis. Radial distribution function of (c) Li-Li distances for all biaxial strains shown together. Black lines (and dark fillings) show the reference state (without strain). Two arrows mark RDF shifts for strains that compress or expand the c axis. Obtained from AIMD simulations at 500 K.

relatable to particular migration pathways, but rather span the whole crystal lattice (see the Supplemental Material, Sec. E [82]). The loosening of this P framework seemed to be consistent with the overall acceleration of different jump types occurring in all three dimensions.

The second feature, which was common to all beneficial strains, was the increased population of short Li-Li distances [below around 3 Å, Fig. 8(c)]. In β -Li₃PS₄, the shortest Li-Li separation was between *8d* and *4b* sites: the average distance was about 3.4 Å and the tail spanned to about 2.5 Å. An increase of the short-bond population was consistent with *c*-axis compression, as it brought the *8d* and *4b* sites closer to each other (the average separation decreased by 1%–2%). The presence of such short Li-Li distances should increase Coulomb repulsion between the *8d* and *4b* sites. As a result, the Li-site energy at *8d* and *4b* sites increased (as presented above) and should contribute to their slight destabilization (as seen in Fig. 7). This increase in site energy should reduce the energy barrier to ion migration, assuming no change in the transition state. Thus, this shortened Li-Li distance could promote Li-ion diffusion and conduction.

An increase of ionic conductivity under compression was reported for several superionic conductors, including Li and Ag conductors [42]. We note that Coulomb repulsion and geometric frustration between ions are the signatures of superionicity [51,55,60,62], and many superionic conductors are reported to have short Li-Li distances [108]. Therefore, it is plausible that compressive strain can increase ionic repulsions and promote diffusion in a variety of superionic conductors (cf. Ref. [120]). Of course, other factors, such as initial occupancies of sites and their connectivity, as well as the mutual orientation of thermal ellipsoids might be important to delineate why some superionic conductors do benefit from compressive strain (e.g., LLZO [41]) and some others do not (e.g., LGPS [36,41]).

4. Strain versus chemical substitution

The magnitude of the strain effect found in this work on Li-ion diffusivity was comparable to that of chemical substitution in β -Li₃PS₄ [63,66,67]. Previous AIMD simulations showed that a nonstoichiometric composition of β -Li₃PS₄ (namely, Li_{2.75}PS₄ or Li_{3.25}PS₄) yielded faster diffusivity, by 1 order of magnitude at 450 K, and better site connectivity due to vacancies or interstitials. In these cases, the degree of correlated motion also increased [63]. Similarly, β -Li₃PS₄ doped with Br and O also showed faster diffusivity, ca. 1 order of magnitude at 450 K for β -Li₃PS_{3.75}O_{0.25} and β -Li_{2.75}PS_{3.75}Br_{0.25}. The Br and O substitution effect was similar to that of the Li nonstoichiometric composition. Near O, a locally lower concentration of Li was established, thus creating a higher concentration of Li ions elsewhere [63]. A twofold conductivity increase was experimentally achieved by Sb₂O₅ substitution of

β -Li₃PS₄ [66] and ZnO substitution of Li₃PS₄ glass [67] at room temperature.

The strain-induced disorder and substitution-induced Li nonstoichiometry had similar effects on the site occupancy, both in terms of the magnitude of the effect and in terms of the mechanism underlying the effect. They both created vacancies at the *8d* and *4b* sites (strain and Li deficiency, e.g., Li_{2.75}PS₄ [63]) or populated the *4c* site (strain and Li surplus, e.g., Li_{3.25}PS₄ [63]), thus increasing the concentration of these active charge carriers and promoting diffusion. Notably, in Ref. [63], variation of the stoichiometry was ± 0.25 Li per formula unit; this corresponded to +25% increase of the *4c* site occupancy, assuming all Li surplus populated the *4c* site; in our biaxially strained supercells, the increase in Li *4c* occupancy was +3% at most, and the respective change of diffusivity was smaller, too.

Since practical solid electrolytes are often nonstoichiometric (i.e., chemically substituted), it is further interesting to assess the effect of strain on diffusivity in nonstoichiometric compositions. We investigated this effect of isotropic strain on the ionic conductivity of Li-deficient and Li-excess compositions, β -Li_{2.94}PS₄ and β -Li_{3.06}PS₄. We intentionally avoided substituted ions to isolate the effect of strain alone, since substitutions could introduce other effects, such as defect association (see the Supplemental Material, Sec. K [82], for further details). Overall, the β -Li_{2.94}PS₄ case was similar to that of β -Li₃PS₄, namely, isotropic compression promoted diffusivity. In β -Li_{2.94}PS₄, the combined effect of a vacancy and compressive strain on diffusivity was 1.79 ± 0.28 times, which was similar to that of strain alone in the stoichiometric case (1.74 ± 0.20 times at 600 K for $\varepsilon = -2\%$). In detail, the introduction of one vacancy sped up diffusivity by 1.36 ± 0.25 times, while subsequent isotropic compression sped up diffusivity further by 1.33 ± 0.25 times. We thus concluded that the net effect of strain was somewhat smaller in the nonstoichiometric case compared with that in the purely stoichiometric compound. This was reasonable, since nonstoichiometry already introduced charge carriers (vacancies), which promoted diffusion. Nevertheless, the effect of strain on the Li-ion diffusivity of β -Li_{2.94}PS₄ was pronounced, and it was as large as the effect of introducing a vacancy alone. Our test calculations on strained β -Li_{3.06}PS₄ showed that the effect of strain on diffusivity was somewhat less perceptible for interstitials (see the Supplemental Material, Sec. K [82]). We note that the investigation of nonstoichiometric compositions under strain is technically complicated, as one must either introduce substituting ions or carry out calculations with charged supercells, which both complicate the analysis. We believe that this analysis can be refined with higher accuracy in future studies, but this level of analysis already indicates that the role of strain can be as important as nonstoichiometry obtained by chemical substitution.

IV. SUMMARY AND REMARKS

We found that elastic strain (biaxial and isotropic) which resulted in c -axis compression in β -Li₃PS₄ facilitated Li-ion conduction, while c -axis tension slowed down Li-ion conduction. The diffusivity increase or decrease with respect to the unstrained state was about twofold at 500 K and was up to about tenfold when extrapolated to room temperature. Overall, β -Li₃PS₄ had a negative activation volume, $\Delta V_a = -2 \text{ cm}^3/\text{mol}$, which was comparable to that in other superionic conductors like β -AgI, Ag₃SI, and Li- β -Al₂O₃ [42]. The magnitude of the strain effect on the activation energy and diffusion was comparable to that in other Li-ion superionic conductors, namely, LGPS [36] and Al-LLZO [41]. The mechanism and the magnitude of the effect of elastic strain on Li-ion diffusion was also comparable to that of chemical substitution in this material [63,66,67].

Compression of the c axis facilitated Li-ion diffusion through increased disorder (higher Li occupancy of the $4c$ site and higher concentration of Li vacancies at the $8d$ and $4b$ sites) in β -Li₃PS₄. The relative increase in conductivity correlated closely with the relative increase in disorder at these sites. The mechanism behind the increased disorder, resulting in increased conductivity with c -axis compression, could be deduced from the decrease of the shortest Li-Li distance ($8d$ - $4b$) seen in the RDF. This increased the Coulomb repulsion between the $8d$ and $4b$ sites and destabilized Li at these sites, thus reducing Li occupancy, resulting in more frequent ion hops. In principle, the short Li-Li distance is a characteristic for many superionic Li-ion conductors [108], while Coulomb repulsion and geometric frustration are well-known signatures of superionicity [51,55,60,62]. These findings indicated that manipulation of Li-Li distances by strain could be used to promote Li disorder and superionic conductivity.

ACKNOWLEDGMENTS

We are grateful to K.J. Van Vliet, Y.-M. Chiang, J. Li, H. Tuller, Y.-T. Chi, R. Park, K. Klyukin, V. Somjit, Y. Dong, and U. Kudu for helpful discussions and suggestions. This work was supported by the Department of Energy, Basic Energy Sciences, under Award No. DE-SC0002633 (Chemomechanics of Far-From-Equilibrium Interfaces). P.Ž. thanks Knut and Alice Wallenberg Foundation scholarship program for supporting his postdoctoral studies at Massachusetts Institute of Technology. Part of the DFT calculations were carried out using (i) the Extreme Science and Engineering Discovery Environment (XSEDE), which is supported by the National Science Foundation (Grant No. ACI-4321548562), and (ii) resources of the National Energy Research Scientific Computing Center (NERSC), a U.S. Department of Energy Office of Science User Facility located at the Lawrence Berkeley National Laboratory, operated under Contract No. DE-AC02-05CH11231.

- [1] J. B. Goodenough and Y. Kim, Challenges for rechargeable Li batteries, *Chem. Mater.* **22**, 587 (2010).
- [2] B. C. H. Steele, Oxygen ion conductors and their technological applications, *Mater. Sci. Eng. B* **13**, 79 (1992).
- [3] P. Ramaswamy, N. E. Wong, and G. K. H. Shimizu, MOFs as proton conductors—challenges and opportunities, *Chem. Soc. Rev.* **43**, 5913 (2014).
- [4] X. Yao, K. Klyukin, W. Lu, M. Onen, S. Ryu, D. Kim, N. Emond, I. Waluyo, A. Hunt, J. A. Del Alamo, and J. Li, Protonic solid-state electrochemical synapse for physical neural networks, *Nat. Commun.* **11**, 1 (2020).
- [5] J. C. Bachman, S. Muy, A. Grimaud, H. H. Chang, N. Pour, S. F. Lux, O. Paschos, F. Maglia, S. Lupart, P. Lamp, and L. Giordano, Inorganic solid-state electrolytes for lithium batteries: Mechanisms and properties governing ion conduction, *Chem. Rev.* **116**, 140 (2016).
- [6] R. Chen, Q. Li, X. Yu, L. Chen, and H. Li, Approaching practically accessible solid-state batteries: Stability issues related to solid electrolytes and interfaces, *Chem. Rev.* **120**, 6820 (2020).
- [7] A. D. Sendek, E. D. Cubuk, E. R. Antoniuk, G. Cheon, Y. Cui, and E. J. Reed, Machine learning-assisted discovery of solid Li-ion conducting materials, *Chem. Mater.* **31**, 342 (2019).
- [8] L. Kahle, A. Marcolongo, and N. Marzari, High-throughput computational screening for solid-state Li-ion conductors, *Energy Environ. Sci.* **13**, 928 (2020).
- [9] S. Wang, Q. Bai, A. M. Nolan, Y. Liu, S. Gong, Q. Sun, and Y. Mo, Lithium chlorides and bromides as promising solid-state chemistries for fast ion conductors with good electrochemical stability, *Angew. Chem.* **131**, 8123 (2019).
- [10] S. W. Bedell, A. Khakifrooz, and D. K. Sadana, Strain scaling for CMOS, *MRS Bull.* **39**, 131 (2014).
- [11] Z. Shi, E. Tsymbalov, M. Dao, S. Suresh, A. Shapeev, and J. Li, Deep elastic strain engineering of bandgap through machine learning, *Proc. Natl. Acad. Sci. U. S. A.* **116**, 4117 (2019).
- [12] Z. Shi, M. Dao, E. Tsymbalov, A. Shapeev, J. Li, and S. Suresh, Metallization of diamond, *Proc. Natl. Acad. Sci. U. S. A.* **117**, 24634 (2020).
- [13] A. Kushima and B. Yildiz, Oxygen ion diffusivity in strained yttria stabilized zirconia: Where is the fastest strain?, *J. Mater. Chem.* **20**, 4809 (2010).
- [14] R. A. de Souza, A. Ramadan, and S. Hörner, Modifying the barriers for oxygen-vacancy migration in fluorite-structured CeO₂ electrolytes through strain: A computer simulation study, *Energy Environ. Sci.* **5**, 5445 (2012).
- [15] B. Yildiz, “Stretching” the energy landscape of oxides—effects on electrocatalysis and diffusion, *MRS Bull.* **39**, 147 (2014).
- [16] J. Wei, D. Ogawa, T. Fukumura, Y. Hirose, and T. Hasegawa, Epitaxial strain-controlled ionic conductivity in Li-ion solid electrolyte Li_{0.33}La_{0.56}TiO₃ thin films, *Cryst. Growth Des.* **15**, 2187 (2015).
- [17] S. Lee, W. Zhang, F. Khatkhatay, Q. Jia, H. Wang, and J. L. MacManus-Driscoll, Strain tuning and strong enhancement of ionic conductivity in SrZrO₃-RE₂O₃ (RE = Sm, Eu, Gd, Dy, and Er) nanocomposite films, *Adv. Funct. Mater.* **25**, 4328 (2015).

- [18] R. E. Newnham, V. Sundar, R. Yimnirun, J. Su, and Q. M. Zhang, Electrostriction: Nonlinear electromechanical coupling in solid dielectrics, *J. Phys. Chem. B* **101**, 10141 (1997).
- [19] A. Banerjee, D. Bernoulli, H. Zhang, M. F. Yuen, J. Liu, J. Dong, F. Ding, J. Lu, M. Dao, W. Zhang, and Y. Lu, Ultralarge elastic deformation of nanoscale diamond, *Science* **360**, 300 (2018).
- [20] J. Christensen and J. Newman, Stress generation and fracture in lithium insertion materials, *J. Solid State Electrochem.* **10**, 293 (2006).
- [21] A. F. Bower, P. R. Guduru, and V. A. Sethuraman, A finite strain model of stress, diffusion, plastic flow, and electrochemical reactions in a lithium-ion half-cell, *J. Mech. Phys. Solids* **59**, 804 (2011).
- [22] J. Tippens, J. C. Miers, A. Afshar, J. A. Lewis, F. J. Q. Cortes, H. Qiao, T. S. Marchese, C. v. di Leo, C. Saldana, and M. T. McDowell, Visualizing chemomechanical degradation of a solid-state battery electrolyte, *ACS Energy Lett.* **4**, 1475 (2019).
- [23] G. G. Amatucci, J. M. Tarascon, and L. C. Klein, CoO_2 , The end member of the Li_xCoO_2 solid solution, *J. Electrochem. Soc.* **143**, 1114 (1996).
- [24] J. Luo, C. Y. Dai, Z. Wang, K. Liu, W. G. Mao, D. N. Fang, and X. Chen, In-situ measurements of mechanical and volume change of LiCoO_2 lithium-ion batteries during repeated charge–discharge cycling by using digital image correlation, *Measurement* **94**, 759 (2016).
- [25] H.-K. Tian, A. Chakraborty, A. A. Talin, P. Eisenlohr, and Y. Qi, Evaluation of the electrochemo-mechanically induced stress in all-solid-state Li-ion batteries, *J. Electrochem. Soc.* **167**, 090541 (2020).
- [26] G. Vardar, W. J. Bowman, Q. Lu, J. Wang, R.J. Chater, A. Aguadero, R. Seibert, J. Terry, A. Hunt, I. Waluyo, D. D. Fong, A. Jarry, E. J. Crumlin, S. L. Hellstrom, Y.-M. Chiang, and B. Yildiz, Structure, chemistry, and charge transfer resistance of the interface between $\text{Li}_7\text{La}_3\text{Zr}_2\text{O}_{12}$ electrolyte and LiCoO_2 cathode, *Chem. Mater.* **30**, 6259 (2018).
- [27] Y. Kim, D. Kim, R. Bliem, G. Vardar, I. Waluyo, A. Hunt, J. T. Wright, J. P. Katsoudas, and B. Yildiz, Thermally driven interfacial degradation between $\text{Li}_7\text{La}_3\text{Zr}_2\text{O}_{12}$ electrolyte and $\text{LiNi}_{0.6}\text{Mn}_{0.2}\text{Co}_{0.2}\text{O}_2$ cathode, *Chem. Mater.* **32**, 9531 (2020).
- [28] S. Hwang, Q. Meng, P. Chen, K. Kisslinger, J. Cen, A. Orlov, Y. Zhu, E. A. Stach, Y. Chu, and D. Su, Strain coupling of conversion-type Fe_3O_4 thin films for lithium ion batteries, *Angew. Chem.* **129**, 7921 (2017).
- [29] H. Fathiannasab, L. Zhu, and Z. Chen, Chemo-mechanical modeling of stress evolution in all-solid-state lithium-ion batteries using synchrotron transmission x-ray microscopy tomography, *J. Power Sources* **483**, 229028 (2021).
- [30] F. Li, J. Li, F. Zhu, T. Liu, B. Xu, T. H. Kim, M. J. Kramer, C. Ma, L. Zhou, and C. W. Nan, Atomically intimate contact between solid electrolytes and electrodes for Li batteries, *Matter* **1**, 1001 (2019).
- [31] J. Chen, L. Yang, Y. Han, Y. H. Bao, K. L. Zhang, X. Li, J. Pang, H. S. Chen, W. L. Song, Y. J. Wei, and D. N. Fang, An in situ system for simultaneous stress measurement and optical observation of silicon thin film electrodes, *J. Power Sources* **444**, 227227 (2019).
- [32] Y. Zhang, Y. Luo, C. Fincher, S. Banerjee, and M. Pharr, Chemo-mechanical degradation in V_2O_5 thin film cathodes of Li-ion batteries during electrochemical cycling, *J. Mater. Chem. A* **7**, 23922 (2019).
- [33] Y. Yang, Q. Wu, Y. Cui, Y. Chen, S. Shi, R.-Z. Wang, and H. Yan, Elastic properties, defect thermodynamics, electrochemical window, phase stability, and Li^+ mobility of Li_3PS_4 : Insights from first-principles calculations, *ACS Appl. Mater. Interfaces* **8**, 25229 (2016).
- [34] A. C. Luntz, J. Voss, and K. Reuter, Interfacial challenges in solid-state Li ion batteries, *J. Phys. Chem. Lett.* **6**, 4599 (2015).
- [35] R. Xu, X. B. Cheng, C. Yan, X. Q. Zhang, Y. Xiao, C. Z. Zhao, J. Q. Huang, and Q. Zhang, Artificial interphases for highly stable lithium metal anode, *Matter* **1**, 317 (2019).
- [36] S. P. Ong, Y. Mo, W. D. Richards, L. Miara, H. S. Lee, and G. Ceder, Phase Stability Electrochemical stability and ionic conductivity of the $\text{Li}_{10\pm 1}\text{MP}_2\text{X}_{12}$ ($\text{M} = \text{Ge}, \text{Si}, \text{Sn}, \text{Al}$ or P , and $\text{X} = \text{O}, \text{S}$ or Se) family of superionic conductors, *Energy Environ. Sci.* **6**, 148 (2013).
- [37] B. Chen, J. Ju, J. Ma, H. Du, R. Xiao, G. Cui, and L. Chen, Strain tunable ionic transport properties and electrochemical window of $\text{Li}_{10}\text{GeP}_2\text{S}_{12}$ superionic conductor, *Comput. Mater. Sci.* **153**, 170 (2018).
- [38] G. F. Harrington, S. Kim, K. Sasaki, H. L. Tuller, and S. Grieshammer, Strain-modified ionic conductivity in rare-earth substituted ceria: Effects of migration direction, barriers, and defect-interactions, *J. Mater. Chem. A* **9**, 8630 (2021).
- [39] T. Mayeshiba and D. Morgan, Strain effects on oxygen migration in perovskites, *Phys. Chem. Chem. Phys.* **17**, 2715 (2014).
- [40] R. H. Radzilowski and J. T. Kummer, The hydrostatic pressure dependence of the ionic conductivity of β -aluminas, *J. Electrochem. Soc.* **118**, 714 (1971).
- [41] A. Moradabadi and P. Kaghazchi, Effect of lattice and dopant-induced strain on the conductivity of solid electrolytes: Application of the elastic dipole method, *Materialia* **9**, 100607 (2020).
- [42] T. Famprakis, O. U. Kudu, J. A. Dawson, P. Canepa, F. Fauth, E. Suard, M. Zbiri, D. Dambournet, O. J. Borkiewicz, H. Bouyanfif, and S. P. Emge, Under pressure: Mechanochemical effects on structure and ion conduction in the sodium-ion solid electrolyte Na_3PS_4 , *J. Am. Chem. Soc.* **142**, 18422 (2020).
- [43] D. Dumett Torres and P. K. Jain, Strain stabilization of superionicity in copper and lithium selenides, *J. Phys. Chem. Lett.* **9**, 1200 (2018).
- [44] J. Hinterberg, T. Zacherle, and R. A. de Souza, Activation Volume Tensor for Oxygen-Vacancy Migration in Strained CeO_2 Electrolytes, *Phys. Rev. Lett.* **110**, 205901 (2013).
- [45] Y. Y. Lin, A. X. bin Yong, W. J. Gustafson, C. N. Reedy, E. Ertekin, J. A. Krogstad, and N. H. Perry, Toward design of cation transport in solid-state battery electrolytes: Structure-dynamics relationships, *Curr. Opin. Solid State Mater. Sci.* **24**, 100875 (2020).

- [46] F. Ning, S. Li, B. Xu, and C. Ouyang, Strain tuned Li diffusion in LiCoO₂ material for Li ion batteries: A first principles study, *Solid State Ionics* **263**, 46 (2014).
- [47] A. Moradabadi, P. Kaghazchi, J. Rohrer, and K. Albe, Influence of elastic strain on the thermodynamics and kinetics of lithium vacancy in bulk LiCoO₂, *Phys. Rev. Mater.* **2**, 015402 (2018).
- [48] C. Tealdi, J. Heath, and M. S. Islam, Feeling the strain: Enhancing ionic transport in olivine phosphate cathodes for Li- and Na-ion batteries through strain effects, *J. Mater. Chem. A* **4**, 6998 (2016).
- [49] M. Jia, H. Wang, Z. Sun, Y. Chen, C. Guo, and L. Gan, Exploring ion migration in Li₂MnSiO₄ for Li-ion batteries through strain effects, *RSC Adv.* **7**, 26089 (2017).
- [50] C. O'Rourke and B. J. Morgan, Interfacial strain effects on lithium diffusion pathways in the spinel solid electrolyte Li-doped MgAl₂O₄, *Phys. Rev. Mater.* **2**, 45403 (2018).
- [51] B. Kozinsky, S. A. Akhade, P. Hirel, A. Hashibon, C. Elsässer, P. Mehta, A. Logeat, and U. Eisele, Effects of Sublattice Symmetry and Frustration on Ionic Transport in Garnet Solid Electrolytes, *Phys. Rev. Lett.* **116**, 055901 (2016).
- [52] M. Yashima, M. Itoh, Y. Inaguma, and Y. Morii, Crystal structure and diffusion path in the fast lithium-ion conductor La_{0.62}Li_{0.16}TiO₃, *J. Am. Chem. Soc.* **127**, 3491 (2005).
- [53] Y. Mo, S. P. Ong, and G. Ceder, First principles study of the Li₁₀GeP₂S₁₂ lithium super ionic conductor material, *Chem. Mater.* **24**, 15 (2012).
- [54] Y. Deng, C. Eames, J. N. Chotard, F. Laleire, V. Seznec, S. Emge, O. Pecher, C. P. Grey, C. Masquelier, and M. S. Islam, Structural and mechanistic insights into fast lithium-ion conduction in Li₄SiO₄-Li₃PO₄ solid electrolytes, *J. Am. Chem. Soc.* **137**, 9136 (2015).
- [55] B. Kozinsky, *Handbook of Materials Modeling*, edited by W. Andreoni, and S. Yip (Springer International Publishing, Cham, 2018), pp. 1–20.
- [56] D. di Stefano, A. Miglio, K. Robeyns, Y. Filinchuk, M. Lechartier, A. Senyshyn, H. Ishida, S. Spannenberger, D. Prutsch, S. Lunghammer, and D. Rettenwander, Superionic diffusion through frustrated energy landscape, *Chem* **5**, 2450 (2019).
- [57] X. He, Y. Zhu, and Y. Mo, Origin of Fast ion diffusion in super-ionic conductors, *Nat. Commun.* **8**, 15893 (2017).
- [58] Z. Zhang, P. N. Roy, H. Li, M. Avdeev, and L. F. Nazar, Coupled cation-anion dynamics enhances cation mobility in room-temperature superionic solid-state electrolytes, *J. Am. Chem. Soc.* **141**, 19360 (2019).
- [59] Z. Zhang, H. Li, K. Kaup, L. Zhou, P. N. Roy, and L. F. Nazar, Targeting superionic conductivity by turning on anion rotation at room temperature in fast ion conductors, *Matter* **2**, 1667 (2020).
- [60] Z. Zou, N. Ma, A. Wang, Y. Ran, T. Song, Y. Jiao, J. Liu, H. Zhou, W. Shi, B. He, and D. Wang, Relationships between Na⁺ distribution, concerted migration, and diffusion properties in rhombohedral NASICON, *Adv. Energy Mater.* **10**, 2001486 (2020).
- [61] B. C. Wood and N. Marzari, Dynamical Structure, Bonding, and Thermodynamics of the Superionic Sublattice in α -AgI, *Phys. Rev. Lett.* **97**, 166401 (2006).
- [62] A. Düvel, P. Heitjans, P. Fedorov, G. Scholz, G. Cibin, A. V. Chadwick, D. M. Pickup, S. Ramos, L. W. Sayle, E. K. Sayle, and T. X. Sayle, Is geometric frustration-induced disorder a recipe for high ionic conductivity?, *J. Am. Chem. Soc.* **139**, 5842 (2017).
- [63] N. J. J. de Klerk, E. van der Maas, and M. Wagemaker, Analysis of diffusion in solid-state electrolytes through MD simulations, improvement of the Li-ion conductivity in β -Li₃PS₄ as an example, *ACS Appl. Energy Mater.* **1**, 3230 (2018).
- [64] R. Mercier, J.-P. Malugani, B. Fahys, G. Robert, and J. Douglade, Structure du tetrathiosphosphate de lithium, *Acta Crystallogr., Sect. B: Struct. Crystallogr. Cryst. Chem.* **38**, 1887 (1982).
- [65] K. Momma and F. Izumi, VESTA3 for three-dimensional visualization of crystal, volumetric and morphology data, *J. Appl. Crystallogr.* **44**, 1272 (2011).
- [66] D. Xie, S. Chen, Z. Zhang, J. Ren, L. Yao, L. Wu, X. Yao, and X. Xu, High ion conductive Sb₂O₅-doped β -Li₃PS₄ with excellent stability against Li for all-solid-state lithium batteries, *J. Power Sources* **389**, 140 (2018).
- [67] G. Liu, D. Xie, X. Wang, X. Yao, S. Chen, R. Xiao, H. Li, and X. Xu, High air-stability and superior lithium ion conduction of Li_{3+3x}P_{1-x}Zn_xS_{4-x}O_x by aliovalent substitution of ZnO for all-solid-state lithium batteries, *Energy Storage Mater.* **17**, 266 (2019).
- [68] Y. H. Han, H. B. Wang, I. A. Troyan, C. X. Gao, and M. I. Eremets, Pressure induced ionic-superionic transition in silver iodide at ambient temperature, *J. Chem. Phys.* **140**, 44708 (2014).
- [69] P. E. Blöchl, Projector augmented-wave method, *Phys. Rev. B* **50**, 17953 (1994).
- [70] J. P. Perdew, K. Burke, and M. Ernzerhof, Generalized Gradient Approximation Made Simple, *Phys. Rev. Lett.* **77**, 3865 (1996).
- [71] J. P. Perdew, K. Burke, and M. Ernzerhof, Erratum: Generalized Gradient Approximation Made Simple [Physical Review Letters (1996) 77 (3865)], *Phys. Rev. Lett.* **78**, 1396 (1997).
- [72] G. Kresse and J. Hafner, *Ab initio* molecular dynamics for liquid metals, *Phys. Rev. B* **47**, 558 (1993).
- [73] G. Kresse and J. Hafner, *Ab initio* molecular-dynamics simulation of the liquid-metalamorphous-semiconductor transition in germanium, *Phys. Rev. B* **49**, 14251 (1994).
- [74] G. Kresse and J. Furthmüller, Efficiency of *ab-initio* total energy calculations for metals and semiconductors using a plane-wave basis set, *Comput. Mater. Sci.* **6**, 15 (1996).
- [75] G. Kresse and J. Furthmüller, Efficient iterative schemes for *ab initio* total-energy calculations using a plane-wave basis set, *Phys. Rev. B: Condens. Matter Mater. Phys.* **54**, 11169 (1996).
- [76] D. Joubert, From ultrasoft pseudopotentials to the projector augmented-wave method, *Phys. Rev. B: Condens. Matter Mater. Phys.* **59**, 1758 (1999).
- [77] K. Homma, M. Yonemura, T. Kobayashi, M. Nagao, M. Hirayama, and R. Kanno, Crystal structure and phase transitions of the lithium ionic conductor Li₃PS₄, *Solid State Ionics* **182**, 53 (2011).

- [78] S. Nosé, A unified formulation of the constant temperature molecular dynamics methods, *J. Chem. Phys.* **81**, 511 (1998).
- [79] W. G. Hoover, Canonical dynamics: Equilibrium phase-space distributions, *Phys. Rev. A* **31**, 1695 (1985).
- [80] M. Parrinello and A. Rahman, Crystal Structure and Pair Potentials: A Molecular-Dynamics Study, *Phys. Rev. Lett.* **45**, 1196 (1980).
- [81] M. Parrinello and A. Rahman, Polymorphic transitions in single crystals: A new molecular dynamics method, *J. Appl. Phys.* **52**, 7182 (1998).
- [82] See the Supplemental Material at <http://link.aps.org/supplemental/10.1103/PRXEnergy.1.023003> for further computational details, data, analysis, and comments.
- [83] H. Flyvbjerg and H. G. Petersen, Error estimates on averages of correlated data, *J. Chem. Phys.* **91**, 461 (1989).
- [84] A. Marcolongo and N. Marzari, Ionic correlations and failure of Nernst-Einstein relation in solid-state electrolytes, *Phys. Rev. Mater.* **1**, 025402 (2017).
- [85] R. E. Jones and K. K. Mandadapu, Adaptive Green-Kubo estimates of transport coefficients from molecular dynamics based on robust error analysis, *J. Chem. Phys.* **136**, 154102 (2012).
- [86] M. Mottet, A. Marcolongo, T. Laino, and I. Tavernelli, Doping in garnet-type electrolytes: Kinetic and thermodynamic effects from molecular dynamics simulations, *Phys. Rev. Mater.* **3**, 035403 (2019).
- [87] W. Tang, E. Sanville, and G. Henkelman, A grid-based Bader analysis algorithm without lattice bias, *J. Condens. Matter Phys.* **21**, 7 (2009).
- [88] R. F. W. Bader, The zero-flux surface and the topological and quantum definitions of an atom in a molecule, *Theor. Chem. Acc.* **105**, 276 (2001).
- [89] Y. Chen, L. Cai, Z. Liu, C. R. de la Cruz, C. Liang, and K. An, Correlation of anisotropy and directional conduction in β -Li₃PS₄ fast Li⁺ conductor, *Appl. Phys. Lett.* **107**, 13904 (2015).
- [90] H. Stöfler, T. Zinkevich, M. Yavuz, A. Senyshyn, J. Kulisch, P. Hartmann, T. Adermann, S. Randau, F. H. Richter, J. Janek, and S. Indris, Li⁺-ion dynamics in β -Li₃PS₄ observed by NMR: Local hopping and long-range transport, *J. Phys. Chem. C* **122**, 15954 (2018).
- [91] P. Haas, F. Tran, and P. Blaha, Calculation of the lattice constant of solids with semilocal functionals, *Phys. Rev. B: Condens. Matter Mater. Phys.* **79**, 085104 (2009).
- [92] K. Kaup, L. Zhou, A. Huq, and L. F. Nazar, Impact of the Li substructure on the diffusion pathways in alpha and beta Li₃PS₄: An *in situ* high temperature neutron diffraction study, *J. Mater. Chem. A* **8**, 12446 (2020).
- [93] M. Tachez, J. P. Malugani, R. Mercier, and G. Robert, Ionic conductivity of and phase transition in lithium thiophosphate Li₃PS₄, *Solid State Ionics* **14**, 181 (1984).
- [94] Z. Liu, W. Fu, E. A. Payzant, X. Yu, Z. Wu, N. J. Dudney, J. Kiggans, K. Hong, A. J. Rondinone, and C. Liang, Anomalous high ionic conductivity of nanoporous β -Li₃PS₄, *J. Am. Chem. Soc.* **135**, 975 (2013).
- [95] Ö. U. Kudu, T. Famprikis, B. Fleutot, M. D. Braidia, T. le Mercier, M. S. Islam, and C. Masquelier, A review of structural properties and synthesis methods of solid electrolyte materials in the Li₂S–P₂S₅ binary system, *J. Power Sources* **407**, 31 (2018).
- [96] C. E. Derrington and M. O’Keeffe, Anion conductivity and disorder in lead fluoride, *Nat. Phys. Sci.* **246**, 44 (1973).
- [97] K. Koto, H. Schulz, and R. A. Huggins, Anion disorder and ionic motion in lead fluoride (β -PbF₂), *Solid State Ionics* **1**, 355 (1980).
- [98] C. Seok and D. W. Oxtoby, Phase transitions in AgI, *Phys. Rev. B* **56**, 11485 (1997).
- [99] P. A. Madden, K. F. O’Sullivan, and G. Chiarotti, Ordering of the silver ions in α -AgI: A mechanism for the α - β phase transition, *Phys. Rev. B* **45**, 10206 (1992).
- [100] H. A. Harwig and A. G. Gerards, Electrical properties of the α , β , γ , and δ phases of bismuth sesquioxide, *J. Solid State Chem.* **26**, 265 (1978).
- [101] C. E. Mohn, S. Stølen, S. T. Norberg, and S. Hull, Oxide-Ion Disorder Within the High Temperature δ Phase of Bi₂O₃, *Phys. Rev. Lett.* **102**, 155502 (2009).
- [102] K. Funke, Solid state ionics: From Michael Faraday to green energy—the European dimension, *Sci. Technol. Adv. Mater.* **14**, 43502 (2013).
- [103] G. K. Phani Dathar, J. Balachandran, P. R. C. Kent, A. J. Rondinone, and P. Ganesh, Li-ion site disorder driven superionic conductivity in solid electrolytes: A first-principles investigation of β -Li₃PS₄, *J. Mater. Chem. A* **5**, 1153 (2017).
- [104] F. Ducastelle, *Order and Phase Stability in Alloys* (North-Holland, Amsterdam, New York, 1991).
- [105] A. I. Kitaigorodskiy, *Order and Disorder in the World of Atoms* (Springer New York, New York, NY, 1967).
- [106] G. J. Redhammer, M. Meven, S. Ganschow, G. Timpelt, and D. Rettenwander, Single-crystal neutron and x-ray diffraction study of garnet-type solid-state electrolyte Li₆La₃ZrTaO₁₂: An *in situ* temperature-dependence investigation ($2.5 \leq T \leq 873$ K), *Acta. Crystallogr. B: Struct. Sci. Cryst. Eng. Mater.* **77**, 123 (2021).
- [107] Y. Wang, M. Klenk, K. Page, and W. Lai, Local structure and dynamics of lithium garnet ionic conductors: A model material Li₅La₃Ta₂O₁₂, *Chem. Mater.* **26**, 5613 (2014).
- [108] X. He, Q. Bai, Y. Liu, A. M. Nolan, C. Ling, and Y. Mo, Crystal structural framework of lithium super-ionic conductors, *Adv. Energy Mater.* **9**, 1902078 (2019).
- [109] S. Hori, S. Taminato, K. Suzuki, M. Hirayama, Y. Kato, and R. Kanno, Structure–property relationships in lithium superionic conductors having a Li₁₀GeP₂S₁₂-type structure, *Acta. Crystallogr. B: Struct. Sci. Cryst. Eng. Mater.* **71**, 727 (2015).
- [110] R. F. W. Bader, *Atoms in Molecules: A Quantum Theory* (Clarendon Press, Oxford, 1990).
- [111] J. Yang and J. S. Tse, First-principles molecular simulations of Li diffusion in solid electrolytes Li₃PS₄, *Comput. Mater. Sci.* **107**, 134 (2015).
- [112] H. D. Lim, X. Yue, X. Xing, V. Petrova, M. Gonzalez, H. Liu, and P. Liu, Designing solution chemistries for the low-temperature synthesis of sulfide-based solid electrolytes, *J. Mater. Chem. A* **6**, 7370 (2018).

- [113] X. He, Y. Zhu, A. Epstein, and Y. Mo, Statistical variances of diffusional properties from *ab initio* molecular dynamics simulations, *Npj Comput. Mater.* **4**, 18 (2018).
- [114] J.-M. Doux, H. Nguyen, D. H. S. Tan, A. Banerjee, X. Wang, E. A. Wu, C. Jo, H. Yang, and Y. S. Meng, Stack pressure considerations for room-temperature all-solid-state lithium metal batteries, *Adv. Energy Mater.* **10**, 1903253 (2020).
- [115] J.-M. Doux, Y. Yang, D. H. S. Tan, H. Nguyen, E. A. Wu, X. Wang, A. Banerjee, and Y. S. Meng, Pressure effects on sulfide electrolytes for all solid-state batteries, *J. Mater. Chem. A* **8**, 5049 (2020).
- [116] G. E. Murch, The haven ratio in fast ionic conductors, *Solid State Ionics* **7**, 177 (1982).
- [117] A. van der Ven, G. Ceder, M. Asta, and P. D. Tapesch, First-principles theory of ionic diffusion with nondilute carriers, *Phys. Rev. B* **64**, 184307 (2001).
- [118] X. Li and N. A. Benedek, Enhancement of ionic transport in complex oxides through soft lattice modes and epitaxial strain, *Chem. Mater.* **27**, 2647 (2015).
- [119] A. Chroneos, B. Yildiz, A. Tarancón, D. Parfitt, and J. A. Kilner, Oxygen diffusion in solid oxide fuel cell cathode and electrolyte materials: Mechanistic insights from atomistic simulations, *Energy Environ. Sci.* **4**, 2774 (2011).
- [120] H. Hoshino, H. Yanagiya, and M. Shimoji, Effect of hydrostatic pressure on the electrical conductivity of Ag_3SBr and $\beta\text{-Ag}_3\text{SI}$, *J. Chem. Soc., Faraday Trans. 1* **70**, 281 (1974).